Electronic Supplementary Material (ESI) for Catalysis Science & Technology.
This journal is © The Royal Society of Chemistry 2023

Post-plasma catalysis: Charge effect on product selectivity in conversion of methane and nitrogen plasma to ethylene and ammonia

Sarojini Tiwari[1†], Saleh Ahmat Ibrahim[2†], Brandon Robinson[1], Siobhan Brown[1], Qiang Wang[3] , Fanglin Che[2,*], Jianli Hu[1,*]

[1]Department of Chemical and Biomedical engineering, West Virginia University, Morgantown, USA

[2]Department of Chemical Engineering, University of Massachusetts Lowell, Lowell, USA

[3]Material Characterization Facilities, West Virginia University, Morgantown, US

† S. Tiwari, S. A. Ibrahim contributed equally.

*Corresponding authors emails: john.hu@mail.wvu.edu; fanglin_che@uml.edu

Supporting information

1. Catalyst Characterization

1.1 XPS survey spectra of fresh and spent Ag-Pd/CeO$_2$

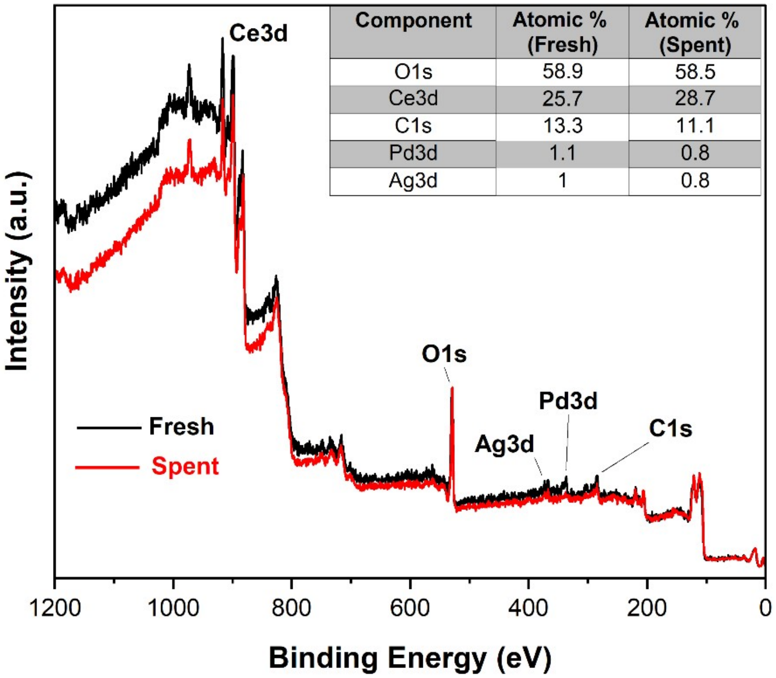

Component	Atomic % (Fresh)	Atomic % (Spent)
O1s	58.9	58.5
Ce3d	25.7	28.7
C1s	13.3	11.1
Pd3d	1.1	0.8
Ag3d	1	0.8

Figure S-1: Survey spectra of fresh and spent Ag-Pd/Ceria with elemental composition on the catalyst surface

1.2 TEM imaging

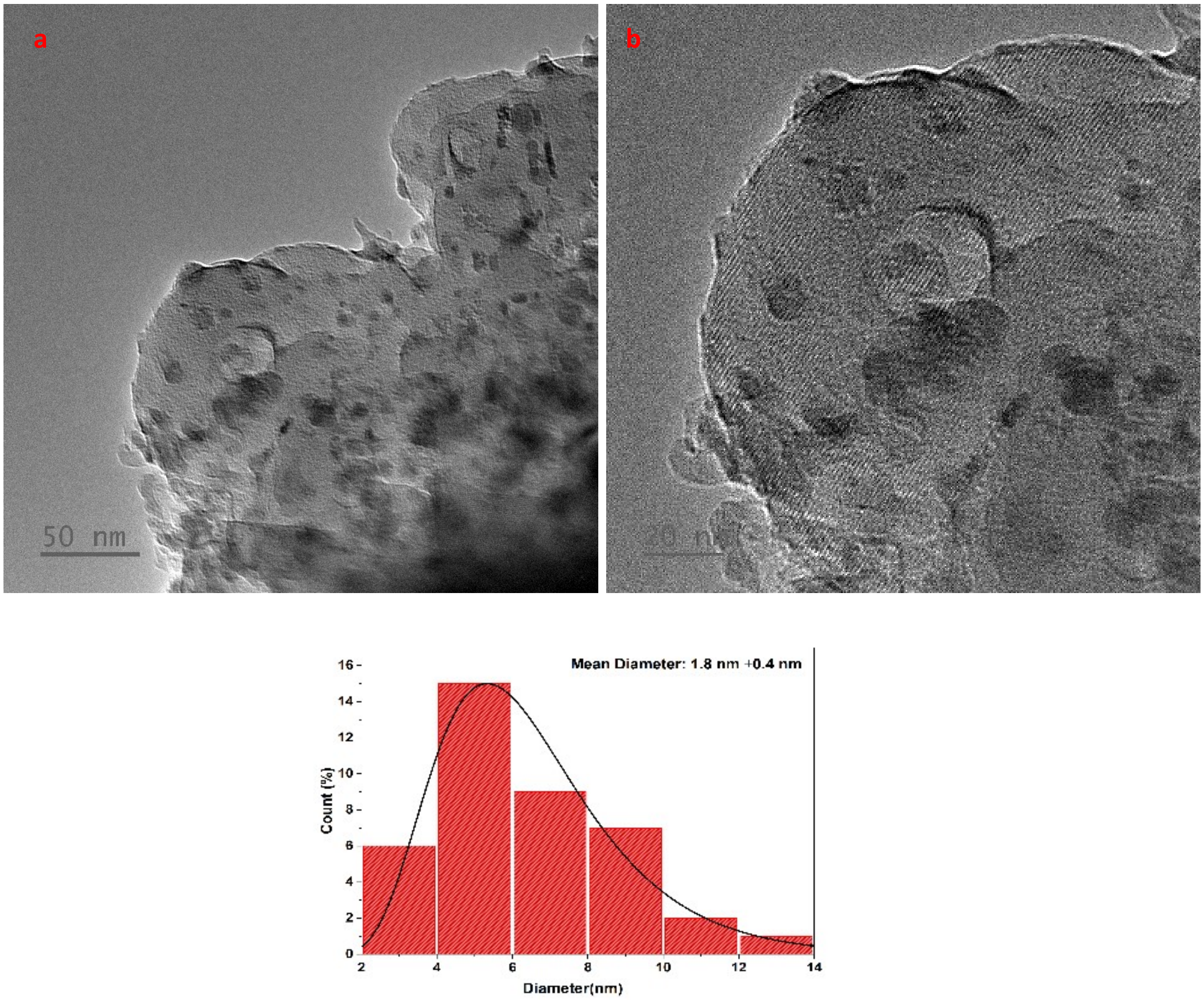

Figure S-2: TEM image of freshly reduced Ag-Pd/ Ceria catalyst at a resolution of 50 nm (a), spent Ag-Pd/Ceria from plasma + catalysts reaction at a resolution 20nm (b)

The high-resolution TEM images of the bimetallic catalyst can be seen in Figure S-2. The particle size distribution was calculated by measuring the diameter of 100 particles randomly selected form the image shown in Figure S-2a. The mean particle size was calculated to be 1.8 nm. As shown in Figure S-2a, the particle distribution is not uniform. The larger metal particles could be due to the aggregation of the metal particles. The typical nano-structure of ceria support is clearly visible in the image obtained at the resolution of 20 nm of the Ag-Pd/ Ceria catalyst (Figure S-2 b).

2. Concentration profile of products

2.1 Production rate in ml/min

The concentration profile of C_2 products, HCN, H_2 and NH_3 in the product gas mixture of all the three set of reactions can be seen in Figure S-3 and S-4.

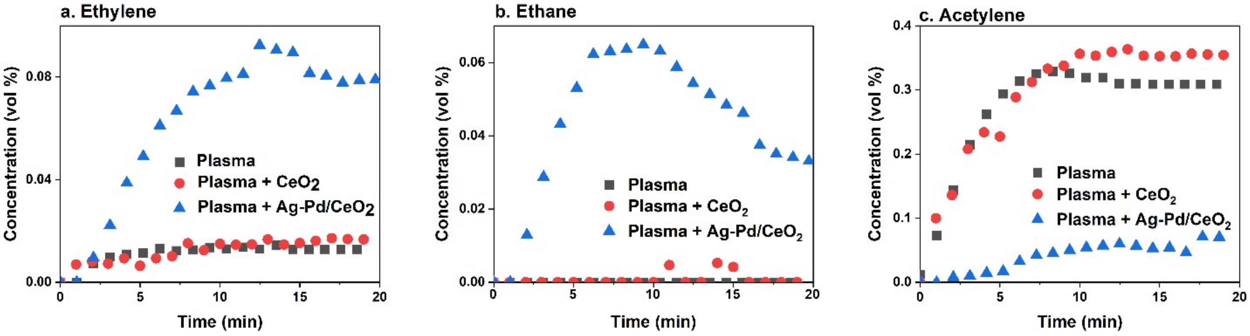

Figure S-3: Production rate of C_2 products in ml/min (a) Ethylene, (b) Ethane, (c) Acetylene

As shown in Figure S-3a, the ethylene production rate is highest in case of plasma + Ag-Pd/CeO_2 reaction stabilizing at around 0.08 % by volume. In case of plasma and plasma + CeO_2, it is produced in very small amount. The production profile of ethane (Figure S-3b) follows similar pattern, stabilizing at around 0.038% in case of plasma+ Ag-Pd/Ceria and absent in the other two reaction scenarios.

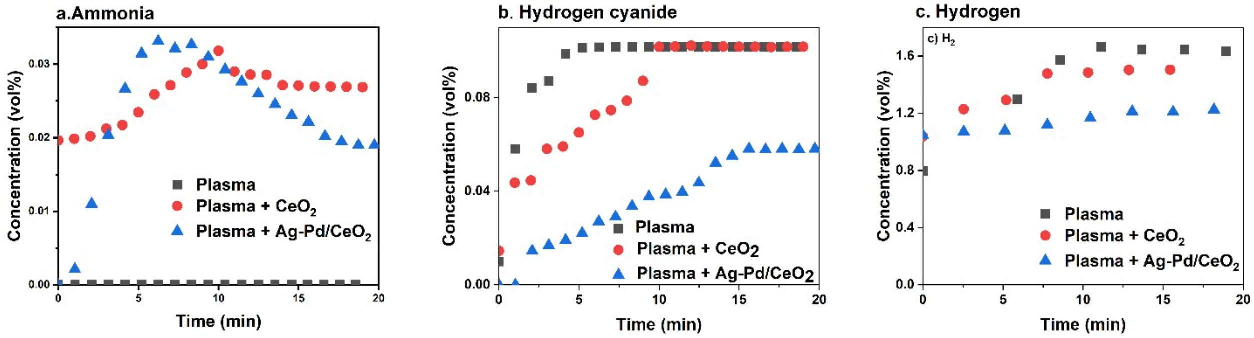

Figure S-4: Production rate of N-containing products and hydrogen in ml/min (a)Ammonia, (b) HCN, (c) Hydrogen

The acetylene production rate is shown in Figure S-3c. In plasma and plasma + CeO_2 reactions, acetylene is the major product stabilizing at around 0.35% by volume. In plasma + Ag-Pd/CeO_2 reaction, the concentration of acetylene is minimum in the product gas mixture. This indicates that the metals Ag-Pd plays an important role in improving the selectivity of ethylene over acetylene and ethane in the product gas mixture. The production profile of ammonia, HCN, and hydrogen is shown in Figure S-4. About 200 ppm of Ammonia is continuously produced in case of plasma + Ag-Pd/CeO_2 reaction (Figure S-4a).

The amount of ammonia produced in plasma + CeO_2 was slightly higher than that of plasma + Ag-Pd/CeO_2 reaction. As shown in Figure S-4b, HCN is produced in equal amounts (~ 0.1%) in both plasma + CeO_2 and plasma reactions. It is reduced to around 0.04% in the plasma + Ag-Pd/CeO_2 reaction. The concentration of hydrogen (Figure S-4c) decreases slightly from 1.6% in case of plasma to 1.5% in plasma + CeO_2 reaction and 1.2% in plasma + Ag-Pd/CeO_2 reaction.

2.2 Absolute selectivity

Table S-1: Absolute selectivity of products

Reaction	**Acetylene**	**Ethylene**	**Ethane**	**HCN**	**Ammonia**	**Hydrogen**
Plasma	16.23	0.62	0	4.87	0	78.28
Plasma + CeO_2	15.48	0.66	0	5.23	1.33	77.29
Plasma+ Ag/Pd-CeO_2	2.51	5.23	2.19	2.88	1.33	85.85
Catalyst	2.96	1.17	15.69	7.58	0	72.61

3. Phase diagram

The phase diagram for the thermodynamic stability of the surface O* in the Ag-Pd system was built in order to calculate the Gibbs free energy (ΔG) of AgPd surface O* reduction ($H_2 + O^* \rightarrow H_2O + *$) as function of H$_2$ partial pressure using DFT. The partial pressure of H$_2$ is further represented by its chemical potential ($\Delta\mu_H$) in the phase diagram [1,2]. The reaction energy of surface O reduction over Ag-Pd catalyst and the Gibbs free energy are calculated using Eqns. (S1)-(S2):

$$\Delta H_{rxn} = E_* + E_{H_2O} - E_{O^*} - E_{H_2} \tag{S1}$$

$$\Delta G = \Delta H_{rxn} + \Delta\mu_{H_2O} - 2\Delta\mu_H \tag{S2}$$

where E_* , E_{O^*}, E_{H_2O} and E_{H_2} represent the Ag-Pd surface energy, the energy of O* adsorption over the AgPd surface, the gas phase energies of H_2O and H_2, respectively. Hydrogen chemical potential $\Delta\mu_H$ is defined by $\Delta\mu_H = \mu_H - \frac{1}{2}E_{H_2}$, where $\mu_H\left(0\,K, p_0^{H_2}\right) = 0 = \frac{1}{2}E_{H_2} = 0$ since H_2 molecule was taken as hydrogen reference at standard pressure conditions. Similarly, the chemical potential of water can be obtained by $\Delta\mu_{H_2O} = \mu_{H_2O} - \frac{1}{2}E_{H_2O}$. Hydrogen chemical potential at certain temperature and pressure is defined by Eqns. (S3)-(S4):

$\Delta\mu_H\left(T, p^{H_2}\right) = \Delta\mu_H\left(T, p_0^{H_2}\right) + \frac{1}{2}k_BTln\frac{p}{p_0}$	(S3)
$\mu_H\left(T, p_0^{H_2}\right) = \frac{1}{2}\left[H\left(T, p_0^{H_2}\right) - H\left(0K, p_0^{H_2}\right)\right] - \frac{1}{2}T\left[S\left(T, p_0^{H_2}\right) - S\left(0K, p_0^{H_2}\right)\right]$	(S4)

here p and p_0 represent the partial pressure and the standard pressure of hydrogen, and k_B stands for Boltzmann's constant. The entropy (S) and enthalpy (H) values of hydrogen and water at atmospheric pressure and different temperatures can be read from thermochemical Tables [3]

The calculated Gibbs free energy of surface O* reduction over the Ag-Pd surface as a function of hydrogen chemical potential at 250 °C is shown in Figure S-5. Our phase diagram shows that under experimental reducing conditions (at 250 ^{o}C and experimental partial pressure of H_2 (5.9 Pa), O^* over Ag-Pd surface is thermodynamically favorable to be reduced since Gibbs free energy (-1.62 eV) is much smaller than 0 eV. This suggests that under the experimental reduction conditions, the Ag-Pd could be maintained metallic.

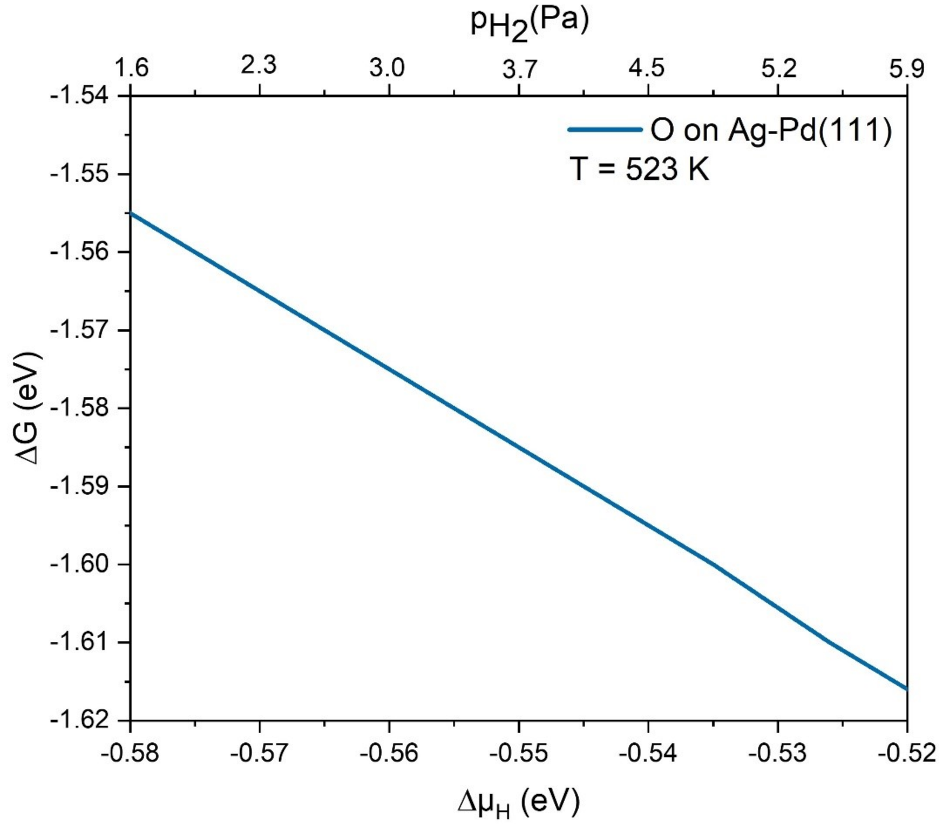

Figure S-5: First principle phase diagram of the thermodynamic equilibrium stabilities of O species over Ag-Pd(111) system as a function of hydrogen chemical potential at 523 K.

4. Computational Setup

DFT calculations with the generalized gradient approximations (GGA)[4,5] and the Perdew-Burke-Ernzerhof (PBE) [4,6–9] exchange correlation functional were used to examine methane dehydrogenation into C_1 or coupling into C_2 hydrocarbon species over the Ag-Pd (111) surface. A four-layer p (4×4) alloy surface was modeled with two bottom layers being fixed to their bulk positions and two top layers being relaxed to electronically interact with the adsorbates. The possible adsorption sites (Figure S-6) of the Ag-

Pd surface include top of Pd, top of Ag, bridge of Pd-Pd, bridge of Ag-Ag, bridge of Pd-Ag, fcc and hcp of Ag-Pd interface sites.

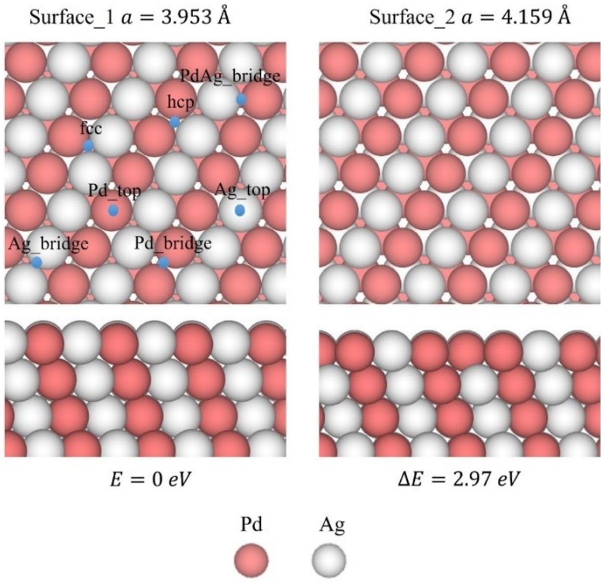

Figure S-6: Top and side views of the catalytic Ag-Pd surface with different lattice constants. The possible adsorption sites over the Ag-Pd surface are marked in blue. The catalytic Ag-Pd surface has seven adsorption sites at which species can adsorb, including top of Pd, top of Ag, bridge of Pd-Pd, bridge of Ag-Ag, bridge of Pd-Ag, hcp, and fcc sites. The surface with lower lattice constant is determined to be the most stable configuration compared to the surface with larger lattice constant.

The energetics of the possible elementary reactions for hydrocarbon synthesis from methane over the Ag-Pd surface were initially conducted without surface charge effects. Based on the energetics of the most favorable reaction pathways, we then polarized alloy surface with positive surface charges and optimized the adsorption/reaction during the hydrocarbon production process. The positive surface charges were ranging from δ^0 to $\delta^{+0.6}$ with $\delta^{+0.1}$ increment was employed. The possible adsorption configurations (Figures S-7 to S-20) for all the species involved in hydrocarbon synthesis from methane over the catalytic Ag-Pd (111) surface were examined. The calculated adsorption energies and site preferences of all the intermediates are presented in Table S-2**.**

5. Adsorption of intermediates during acetylene, ethylene, and ethane synthesis from methane conversion

5.1 Hydrogen (H) and Carbon (C)

The preferred adsorption sites for H and C species are the hcp site, with an associated adsorption energies of -2.62 eV and -7.12 eV, respectively. H and C species are not stable on the top Pd, top of Ag and the bridge sites of both Ag-Ag and Pd-Pd surfaces. Furthermore, when adsorbed on these sites, they shift to the most stable fcc and hcp sites, respectively.

Table S-2. Summary of the adsorption energies of hydrocarbon species over Ag-Pd (111)

Species	Site preference	Adsorption energy (eV)	Ref.
H	hcp	-2.62	-2.67[a]
C	hcp	-7.12	-5.67[b]
CH	hcp	-5.30	-5.75[b]
CH_2	Pd-Pd bridge	-4.18	-3.78[b]
CH_3	Pd-top	-1.56	-1.67[a]
CH_4	Ag-top	-0.02	-
H_2	hcp	-0.02	-
C_2	Ag-Ag bridge	-4.70	-
C_2H	fcc	-4.40	-4.4[a]
C_2H_2	hcp	-1.07	-1.30[a]
C_2H_3	Pd-Pd bridge	-2.53	-
C_2H_4	Pd-top	-0.56	-0.72[a]
C_2H_5	Pd-top	-1.36	-1.39[a]
C_2H_6	Ag-top	-0.04	-0.05[a]

[a] From ref. 12. [b] From ref. 13. The difference in the reported binding energies of C, CH and CH_2 species is because ref. 12. and ref. 13. used PW91 functional for the exchange correlation potential and the alloy system was modeled using a 2x2 super cell surface.

5.2 Methylidyne (CH), methylene (CH_2), methyl (CH_3) and methane (CH_4)

DFT calculations revealed that the most favorable site of methylidyne (CH) is the hcp site with an adsorption energy of -5.30 eV. Additionally, methylene (CH_2) species interact strongly at the bridge site of Pd-Pd surface, and methyl (CH_3) adsorbs at the top site of Pd with the corresponding adsorption energies of -4.18 eV and -1.56 eV, respectively. Methane (CH_4) species binds preferably at the Ag top site with an associated adsorption energy of -0.02 eV.

When CH_2 adsorbed at the top of Pd, top of Ag, bridge of Ag-Ag, bridge of Ag-Pd, fcc and hcp sites, they are not stable, and they shift to the most favorable bridge of Pd-Pd site with the binding energy of -4.18 eV. CH_3 species at the top site of Pd bound strongly with the surface. However, CH_4 intermediates have weaker interactions with the Ag-Pd surface, adsorbing at Pd top with an adsorption energy of 0.01 eV.

5.3 Ethyne (C_2H_2), ethylenyl (C_2H_3), ethene (C_2H_4), ethyl (C_2H_5) and ethane (C_2H_6)

The most favorable adsorption site of C_2H_2 is the hcp site of the Ag-Pd(111) surface with an adsorption energy of -1.07 eV. C_2H_3 and C_2H_4 preferably adsorbed at the bridge of Pd-Pd and the Pd-top sites with the corresponding binding energies of -2.53 eV and -0.56 eV, respectively. Moreover, C_2H_5 favorably adsorbed at the Pd-top site with an adsorption energy of -1.36 eV. C_2H_6 interacted weakly with the surface with an associated binding energy of -0.04 eV. The calculated adsorption energies for all the species are in agreement with literature studies [5,10–16].

The dependence of surface positive charges on the reaction energies for all the intermediates involved in methane decomposition is shown in Figures S21, S22. The reaction energies of all the possible elementary reactions that took place during hydrocarbon synthesis from methane conversion were presented in Table S-3. Additionally, the reaction rate constants, collected from literature [17, 18], for the relevant elementary steps are listed in Table S-3. The energy diagram (Figure S-23) of methane dissociation into C_1 or coupling into C_2 hydrocarbon species over the Ag-Pd (111) surface were conducted with and without positive surface charge effects.

Table S-3. The reaction energies of elementary reactions with and without surface charge (δ) effects and the reaction rate constants (k)

Elementary Reactions	δ^0	$\delta^{+0.6}$	δ^0
	ΔH_{rxn} **(eV)**		k (s^{-1})
$CH_4 + CH_4 \rightarrow CH_4 + CH_3 + H$	0.56	0.55	6.4×10^{-5} [a]
$CH_4 + CH_3 + H \rightarrow CH_3 + CH_3 + 2H$	0.56	0.55	6.4×10^{-5} [a]
$CH_3 + CH_3 + 2H \rightarrow CH_3 + CH_2 + 3H$	0.50	0.51	3.9×10^{9} [a]
$CH_3 + CH_2 + 3H \rightarrow CH_2 + CH_2 + 4H$	0.50	0.51	3.9×10^{9} [a]
$CH_2 + CH_2 + 4H \rightarrow CH_2 + CH + 5H$	0.31	0.34	2.7×10^{11} [a]
$CH_2 + CH + 5H \rightarrow CH + CH + 6H$	0.31	0.34	2.7×10^{11} [a]
$CH + CH + 6H \rightarrow CH + C + 7H$	0.57	0.74	4.6×10^{5} [a]
$CH + C + 7H \rightarrow C + C + 8H$	0.57	0.74	4.6×10^{5} [a]
$2C + 8H \rightarrow C_2 + 8H$	-0.38	-0.18	–
$C_2 + 8H \rightarrow C_2H + 7H$	-1.2	-1.7	–
$CH + C + 7H \rightarrow C_2H + 7H$	-1.0	-1.1	–
$C_2H + 7H \rightarrow C_2H_2 + 6H$	-0.10	-0.27	6.6×10^{12} [b]
$CH + CH \rightarrow C_2H_2$	-0.55	-0.66	1.8×10^{12} [b]
$C_2H_2 + H \rightarrow C_2H_3$	-0.82	-0.74	1.7×10^{12} [b]
$C_2H_3 + H \rightarrow C_2H_4$	-0.72	-0.81	1.1×10^{13} [b]
$C_2H_4 + H \rightarrow C_2H_5$	0.02	0.0	9.8×10^{12} [b]
$C_2H_5 + H \rightarrow C_2H_6$	-0.56	-0.42	2.6×10^{11} [b]
$CH_2 + CH \rightarrow C_2H_3$	-1.1	-1.1	–
$CH_2 + CH_2 \rightarrow C_2H_4$	-1.5	-1.5	2.4×10^{12} [b]
$CH_3 + CH_2 \rightarrow C_2H_5$	-0.97	-1.0	–
$CH_3 + CH_3 \rightarrow C_2H_6$	-1.0	-0.93	3.7×10^{12} [b]
$C_2 + 8H \rightarrow C_2 + 4H_2$	2.8	2.4	–
$C_2H_2 + 6H \rightarrow C_2H_2 + 3H_2$	2.1	1.8	–
$C_2H_4 + 4H \rightarrow C_2H_4 + 2H_2$	1.4	1.2	–
$C_2H_6 + 2H \rightarrow C_2H_6 + H_2$	0.69	0.60	–

[a] From ref. 17. [b] From ref. 18. The reaction rate constants for the first eight elementary reactions are collected from reference 17. The rate constants for the dehydrogenation reactions and C_1-C_2 coupling are calculated using data provided in reference 18.

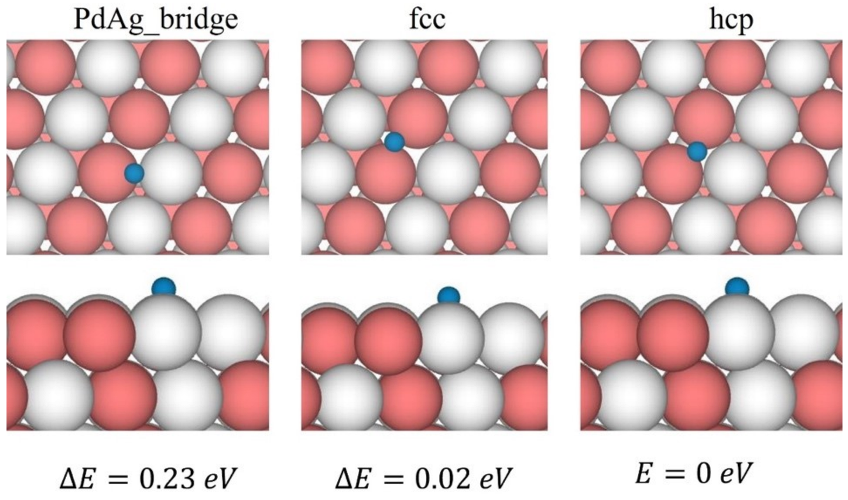

Figure S-7. Top and side views of atomic adsorbate H^* on all the possible adsorption sites and their corresponding binding energies. The adsorbate binds strongly at the catalytic surface Ag-Pd when H^* sits at the hcp. H^* species are not stable at the top of Pd, top of Ag, the bridge of Pd-Pd, the bridge of Ag-Ag and the bridge of Ag-Pd sites and they shift to the most stable configuration hcp. Here, $*$ describes a vacant surface site and M^* stands for species M adsorbed on a surface site.

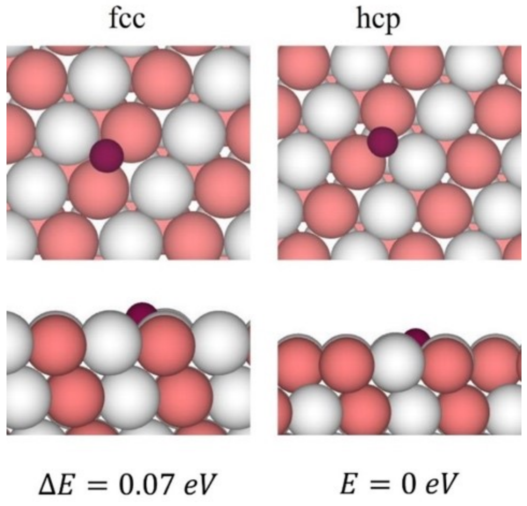

Figure S-8. Top and side views of atomic adsorbate C^* on all the possible adsorption sites and their corresponding binding energies. The adsorbate binds strongly at the catalytic Ag-Pd surface when C^* sits at the hcp. C^* species are not stable at the top of Pd, top of Ag, the bridge of Pd-Pd, the bridge of Ag-Ag and the bridge of Ag-Pd sites and they shift to the most stable geometry fcc and hcp, respectively.

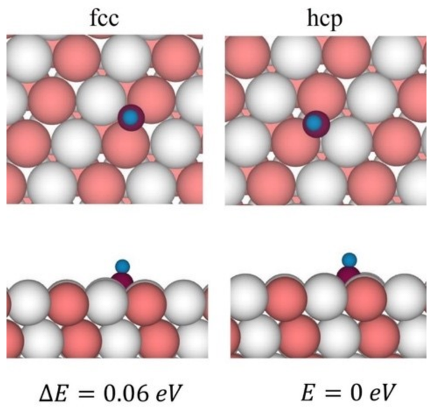

Figure S-9. Top and side views of CH^* intermediates on all the possible adsorption sites and their corresponding binding energies. The adsorbate binds strongly at the catalytic Ag-Pd surface when CH^* sits at the hcp. CH^* species are not stable at the top of Pd, top of Ag, the bridge of Pd-Pd, the bridge of Ag-Ag and the bridge of Ag-Pd sites and they shift to the most stable fcc and hcp sites, respectively.

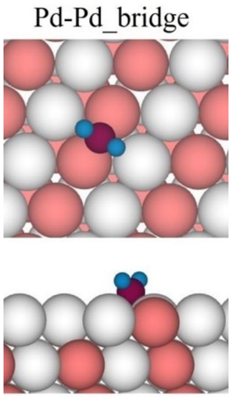

Figure S-10. Top and side views of CH_2^* species on the Pd-Pd bridge adsorption site and its corresponding binding energies. CH_2^* species are not stable at the top of Pd, the top of Ag, fcc and hcp sites. When CH_2^* species are adsorbed on the top of Pd, top of Ag, fcc and hcp sites, they move to the Pd-Pd bridge which is the most stable configuration.

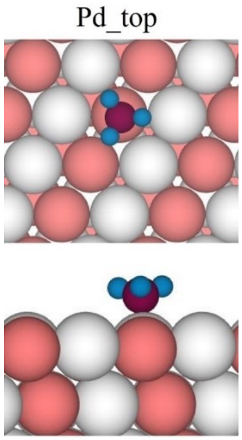

Figure S-11. Top and side views of CH_3^* species on the Pd_top adsorption site and its corresponding adsorption energies. CH_3^* species are not stable at the top of Ag, bridge of Pd-Pd, bridge of Ag-Ag, bridge of Ag-Pd, fcc and hcp sites. When

CH_3^* species are adsorbed at the top of Ag, bridge of Pd-Pd, bridge of Ag-Ag, bridge of Ag-Pd, fcc and hcp sites, they move to the top of Pd, which is the most preferrable configuration.

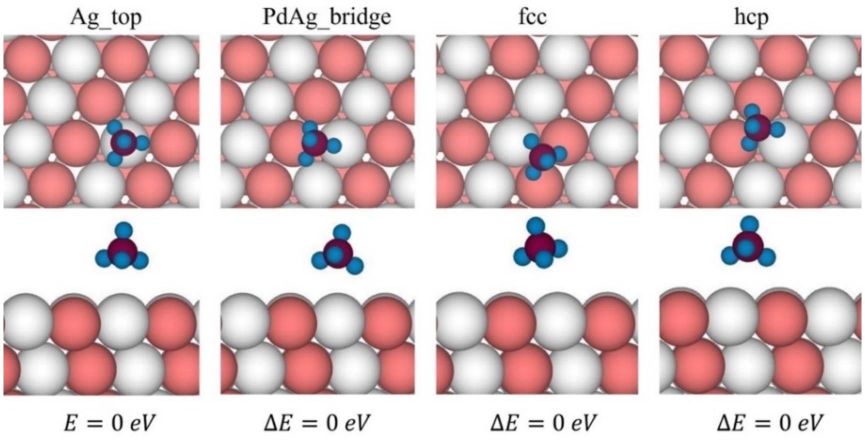

Figure S-12. Top and side views of CH_4^* species on all the possible adsorption sites and the related binding energies. The adsorbate binds strongly at the catalytic Ag-Pd surface when CH_4^* sits at the Ag_top. CH_4^* species are not stable at the top of Pd, bridge of Pd-Pd, bridge of Ag-Ag, bridge of Ag-Pd, fcc, and hcp sites.

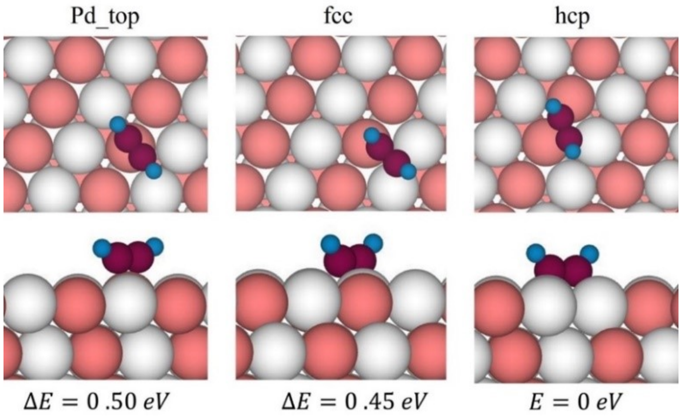

Figure S-13. Top and side views of $C_2H_2^*$ species on all the possible adsorption sites and their corresponding binding energies. The adsorbate binds strongly at the catalytic Ag-Pd surface when $C_2H_2^*$ sits at the hcp. $C_2H_2^*$ species are not stable at the top of Ag, bridge of Pd-Pd, bridge of Ag-Ag, bridge of Ag-Pd, fcc and hcp sites. When $C_2H_2^*$ species are adsorbed at those sites, they move to the hcp which is the most stable configuration.

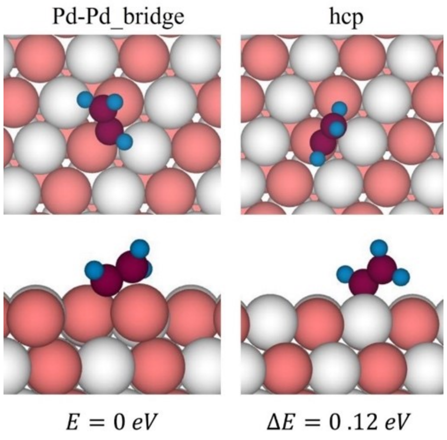

Figure S-14. Top and side views of $C_2H_3^*$ species on all the possible adsorption sites and their corresponding binding energies. The adsorbate binds strongly at the catalytic Ag-Pd surface when $C_2H_3^*$ sits at the Pd-Pd_bridge. $C_2H_3^*$ species are not stable at the top Pd, top of Ag, bridge of Ag-Ag, bridge of Ag-Pd, and fcc sites. When $C_2H_3^*$ species are adsorbed at those sites, they move to the Pd-Pd_bridge which is the most favorable configuration.

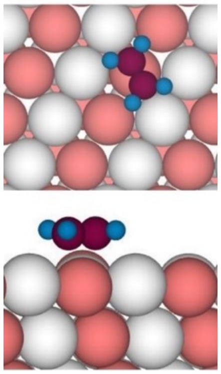

Figure S-15. Top and side views of $C_2H_4^*$ species on the Pd_top adsorption site and its corresponding binding energies. $C_2H_4^*$ species are not stable at the top of Ag, bridge of Pd-Pd, bridge of Ag-Ag, bridge of Ag-Pd, fcc and hcp sites. When $C_2H_4^*$ species are adsorbed at the top of Ag, bridge of Pd-Pd, bridge of Ag-Ag, bridge of Ag-Pd, fcc and hcp sites, they move to the top of Pd which is the most stable configuration.

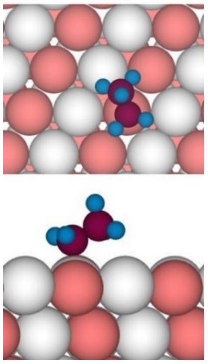

Figure S-16. Top and side views of $C_2H_5^*$ species on the Pd_top adsorption site and its corresponding binding energies. $C_2H_5^*$ species are not stable at the top of Ag, bridge of Pd-Pd, bridge of Ag-Ag, bridge of Ag-Pd, fcc and hcp sites. When $C_2H_5^*$ species are adsorbed at the top of Ag, bridge of Pd-Pd, bridge of Ag-Ag, bridge of Ag-Pd, fcc and hcp sites, they move to the top of Pd which is the most stable configuration.

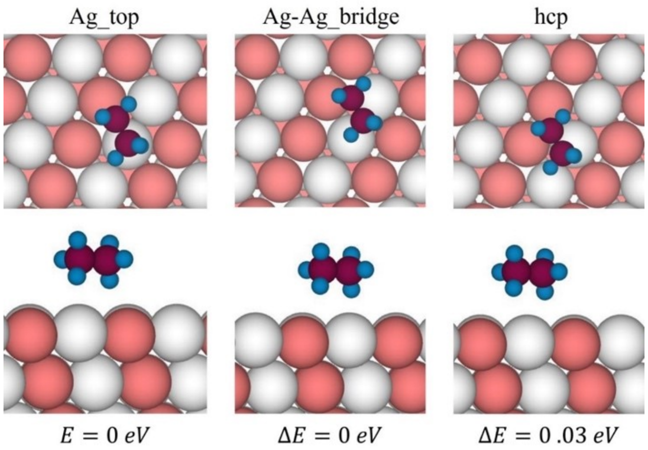

Figure S-17. Top and side views of $C_2H_6^*$ species on all the possible adsorption sites and their corresponding binding energies. The adsorbate binds strongly at the catalytic Ag-Pd surface when $C_2H_6^*$ sits at the top of Ag. $C_2H_6^*$ species are not stable at the fcc site. When $C_2H_6^*$ species are adsorbed at the fcc site, they move to the top of Ag, which is the most stable configuration.

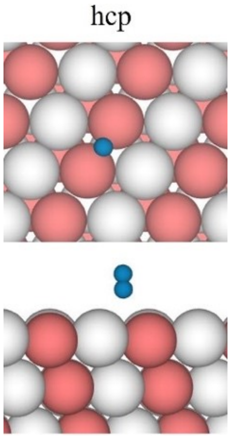

Figure S-18. The adsorption geometry of H_2^* over Ag-Pd surface. The stable configuration is only when H_2^* sits at the hcp site. H_2^* species are not stable at the top of Ag, top of Pd, bridge of Pd-Pd, bridge of Ag-Ag, bridge of Ag-Pd and fcc sites.

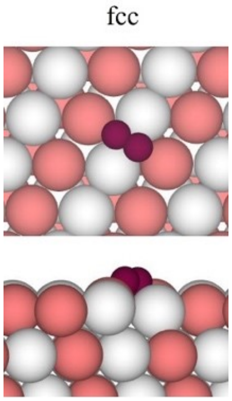

Figure S-19. The adsorption geometry of C_2^* over Ag-Pd surface. The stable configuration is only when C_2^* sits at the fcc site. C_2^* species are not stable at the top of Ag, top of Pd, bridge of Pd-Pd, bridge of Ag-Ag, bridge of Ag-Pd and hcp sites.

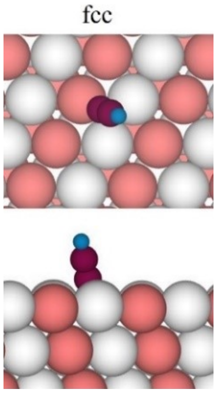

Figure S-20. The adsorption geometry of C_2H^* over Ag-Pd surface. The stable configuration is only when C_2H^* sits at the fcc site. C_2H^* species are not stable at the top of Ag, top of Pd, bridge of Pd-Pd, bridge of Ag-Ag, bridge of Ag-Pd and hcp sites.

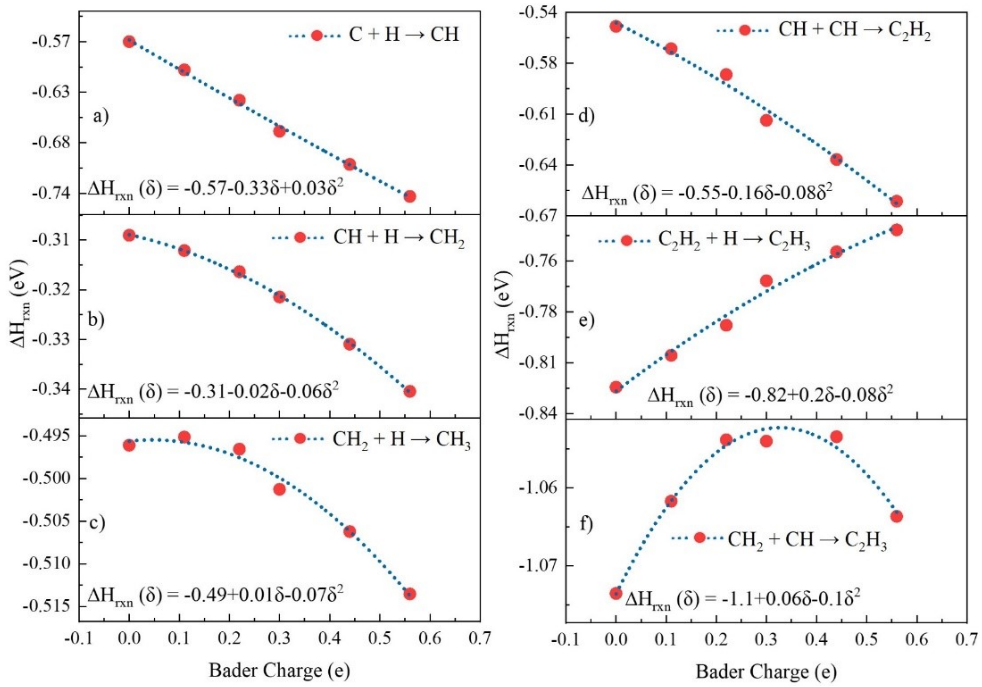

Figure S-21. The surface positive charge effects on the most stable co-adsorption configurations of a C^* and H^*, b CH^* and H^*, c CH_2^* and H^*, d CH^* and CH^*, e $C_2H_2^*$ and H^* and f CH_2^* and CH^* species over the Ag-Pd(111) surface

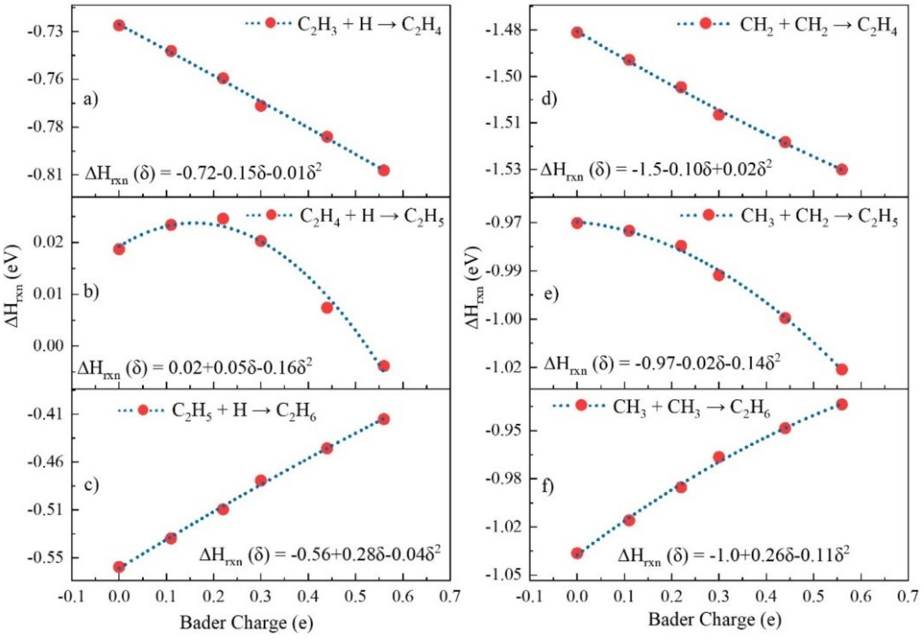

Figure S-22. The positive surface charge effects on the most stable co-adsorption configurations of a $C_2H_3^*$ and H^*, b $C_2H_4^*$ and H^*, c $C_2H_5^*$ and H^*, d CH_2^* and CH_2^*, e CH_3^* and CH_2^* and f CH_3^* and CH_3^* species over the Ag-Pd(111) surface.

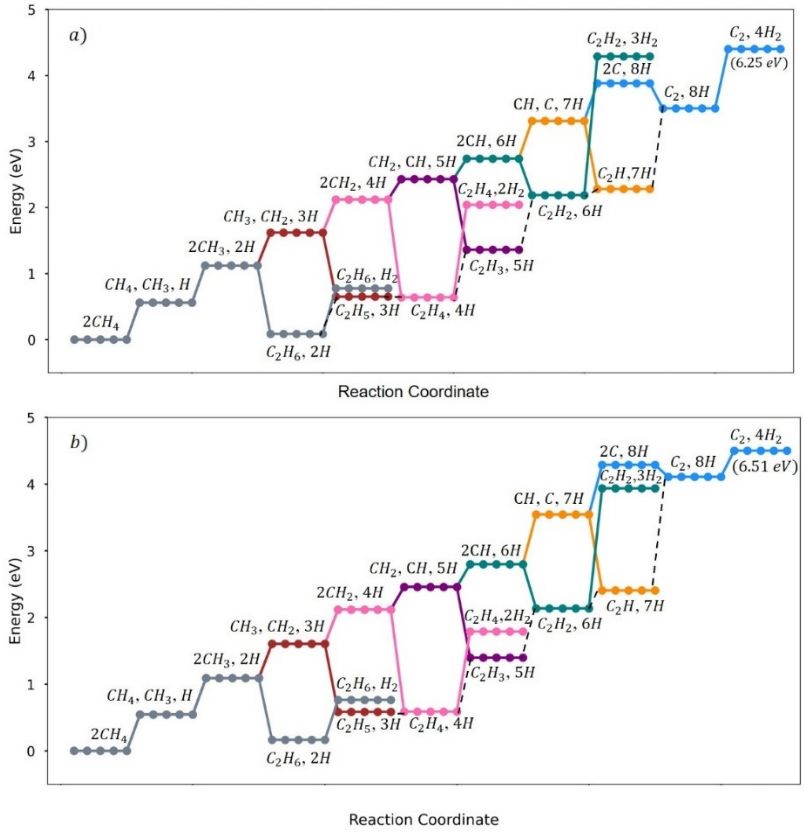

Figure S-23: DFT calculations on revealing the role of positively charged surface for the C_2H_2, C_2H_4 and C_2H_6 formation from methane conversion. a) Energy diagram of methane decomposition into C_1 or coupling into C_2 hydrocarbon species over the Ag-Pd (111) surface without surface positive charge effects and b) under the positive surface charge of +0.6.

6. Carbon (C) and nitrogen (N) component balance

Reaction	**C_{feed} (µmoles)**	**$C_{product}$ (µmoles)**	**N_{feed} (µmoles)**	**$N_{product}$ (µmoles)**
Plasma	44.64	35.70	89.28	88.96
Plasma + CeO_2	44.64	36.83	89.28	89.53
Plasma + Ag-Pd/CeO_2	44.64	19.53	89.28	85.23

Carbon balance was calculated using the following equations:

$$C_{feed}\,(\mu\text{moles}) = [\,(C_{CH4,\ feed} \times F_{feed}) / (22.4\times100 \times 1000)] \times 10\text{\^{}}6 \qquad \text{S5}$$

$$C_{i,m}\,(\text{moles}) = C_i\,(\text{ml/min})/\,(22.4 \times 1000) \qquad \text{S6}$$

where, $C_{CH4,\ feed}$ is the methane feed concentration in volume %, and F_{feed} is the inlet flow rate.

C_i and $C_{i,m}$ are the concentration of C-containing product 'i' in ml/min and moles/min, respectively.

The products 'i' = C_2H_4, C_2H_6, C_2H_2, and HCN

The carbon content of the products was calculated using equation S7:

$$C_{products}\,(\mu\text{moles}) = 2 \times (C_{C2H2,m} + C_{C2H4,m} + C_{C2H6,m}) + C_{HCN,m} \qquad \text{S7}$$

Nitrogen balance was calculated using the following equations:

$$N_{feed}\,(\mu\text{moles}) = [\,(C_{N2,\ feed} \times F_{feed}) / (22.4\times100 \times 1000)] \times 10\text{\^{}}6 \qquad \text{S8}$$

$$C_{j,m}\,(\text{moles}) = C_j\,(\text{ml/min})/\,(22.4 \times 1000) \qquad \text{S9}$$

where, $C_{N2,\ feed}$ is the nitrogen feed concentration in volume %, and F_{feed} is the inlet flow rate.

C_j and $C_{j,m}$ are the concentration of N-containing product 'j' in ml/min and moles/min, respectively.

The products 'j' = HCN, NH_3, and unconverted N_2.

The nitrogen content of the products was calculated using equation S10:

$$N_{products}\,(\mu\text{moles}) = 2 \times (C_{N2,m}\,) + C_{HCN,m} + C_{NH3,m} \qquad \text{S10}$$

All the gaseous products were assumed to be at standard temperature and pressure. The concentration in mole/µmoles were calculated for a duration of one minute.

7. Experimental set-up

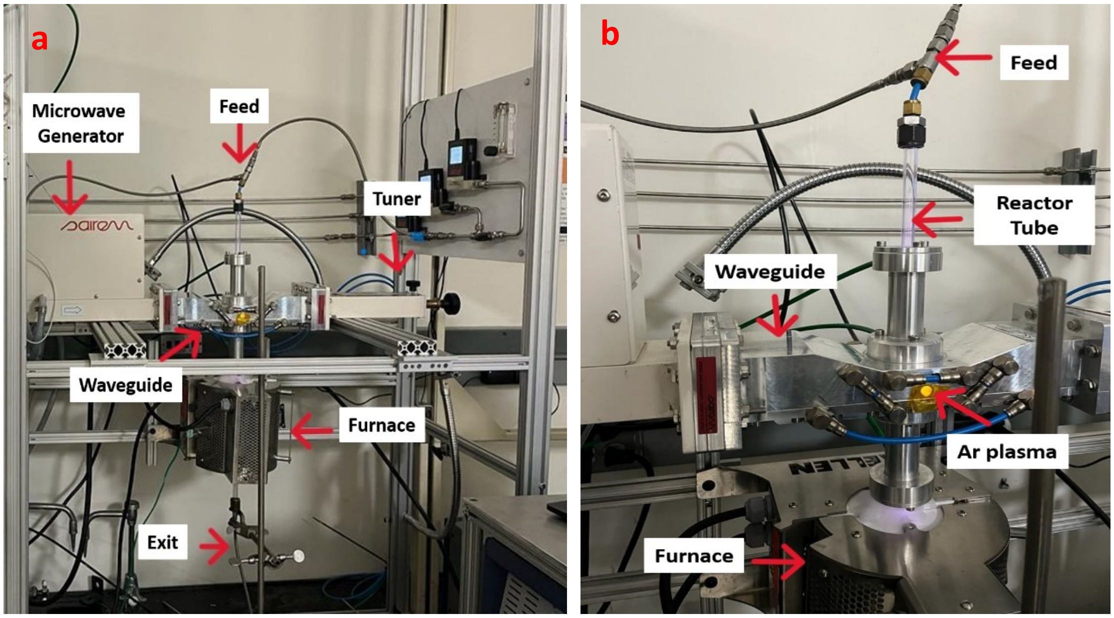

Figure S-24: Picture of the experimental setup (a), close-up of the Ar plasma generated in a quartz tube(b*)*

References

[1] F. Che, S. Ha, J.-S. McEwen, Elucidating the field influence on the energetics of the methane steam reforming reaction: A density functional theory study, Appl Catal B. 195 (2016) 77–89. https://doi.org/https://doi.org/10.1016/j.apcatb.2016.04.026.

[2] J.S. McEwen, T. Anggara, W.F. Schneider, V.F. Kispersky, J.T. Miller, W.N. Deglass, F.H. Riberio, Integrated operando X-ray absorption and DFT characterization of Cu–SSZ-13 exchange sites during the selective catalytic reduction of NOx with NH3, Catal Today. 184 (2012) 129–144. https://www.sciencedirect.com/science/article/pii/S0920586111008510 (accessed February 11, 2023).

[3] M.W. Chase, Nationl Information Standards Organisation (US). NIST-JANAF thermochemical tables. , American Chemical Society, Washington, DC, 1998. https://library.naist.jp/opac/en/book/19856 (accessed February 11, 2023).

[4] G. Kresse, J. Furthmü, Efficient iterative schemes for ab initio total-energy calculations using a plane-wave basis set, Phys Rev B. 54 (1996) 11 169-11 186. https://doi.org/https://doi.org/10.1103/PhysRevB.54.11169.

[5] N. Luo, Z. Hou, G.-L. Chai, Density functional theory study of CH4 dissociation and CC coupling on W-terminated WC (0001) surface, Appl Surf Sci. 591 (2022) 143128.

https://www.sciencedirect.com/science/article/pii/S0169433222006924 (accessed August 9, 2022).

[6] P. Deshlahra, E.E. Wolf, W.F. Schneider, A periodic density functional theory analysis of CO chemisorption on Pt (111) in the presence of uniform electric fields, Journal of Physical Chemistry A. 113 (2009) 4125–4133. https://doi.org/10.1021/jp810518x.

[7] M.C. Payne, M.P. Teter, D.C. Allan, T.A. Arias, J.D. Joannopoulos, Iterative minimization techniques for ab initio total-energy calculations: Molecular dynamics and conjugate gradients, Rev Mod Phys. 64 (1992) 1045–1097. https://doi.org/10.1103/REVMODPHYS.64.1045.

[8] J.P. Perdew, K. Burke, M. Ernzerhof, Generalized gradient approximation made simple, Phys Rev Lett. 77 (1996) 3865–3868. https://doi.org/10.1103/PHYSREVLETT.77.3865.

[9] J. White, D. Bird, Implementation of gradient-corrected exchange-correlation potentials in Car-Parrinello total-energy calculations, Phys Rev B. 50 (1994) 4954. https://journals.aps.org/prb/abstract/10.1103/PhysRevB.50.4954 (accessed August 5, 2022).

[10] F. Che, R. Zhang, J.A. Hensley, S. Ha, J.-S. McEwen, Density functional theory studies of methyl dissociation on a Ni (111) surface in the presence of an external electric field, Physical Chemistry Chemical Physics. 16 (2014) 2399–2410. https://doi.org/https://doi.org/10.1039/C3CP54135E.

[11] M. Petersen, S. Jenkins, D.K.-T.J. of Physical, undefined 2004, Theory of Methane Dehydrogenation on Pt{110}(1 × 2). Part II: Microscopic Reaction Pathways for CHx → CHx-1 (x = 1−3), ACS Publications. 108 (2004) 5920–5929. https://doi.org/10.1021/jp037881r.

[12] Q. Qi, X. Wang, L. Chen, B. Li, Methane dissociation on Pt (1 1 1), Ir (1 1 1) and PtIr (1 1 1) surface: A density functional theory study, Appl Surf Sci. 284 (2013) 784–791. https://www.sciencedirect.com/science/article/pii/S0169433213014864 (accessed August 5, 2022).

[13] W. Baojun, L. Song, R. Zhang, The dehydrogenation of CH4 on Rh (1 1 1), Rh (1 1 0) and Rh (1 0 0) surfaces: A density functional theory study, Appl Surf Sci. 258 (2012) 3714–3722. https://www.sciencedirect.com/science/article/pii/S0169433211019039?casa_token=ZU7SJygRaUQAAAAA:FeOyhtMSCU13I8lBn5QDn9yrxR1N0RpbG5FHu8WtfLYWHrxJQYZAW9eksV2nXyGkrIqhQI05lw (accessed August 5, 2022).

[14] T.L.M. Pham, E.G. Leggesse, J.C. Jiang, Ethylene formation by methane dehydrogenation and C–C coupling reaction on a stoichiometric IrO 2 (110) surface–a density functional theory investigation, Catal Sci Technol. 5 (2015) 4064–4071. https://doi.org/10.1039/x0xx00000x.

[15] D. Mei, M. Neurock, C. Smith, Hydrogenation of acetylene–ethylene mixtures over Pd and Pd–Ag alloys: First-principles-based kinetic Monte Carlo simulations, Jornal of Catalysis. 282 (2009) 181–195. https://www.sciencedirect.com/science/article/pii/S0021951709002978?casa_token=OKPk48U98McAAAAA:hdHz8G5qd1URwQIiUji7aRPcWD8MHQND9926po7orh5FOYCbB08NAjtgM3j4BMExx_3XCv0ZgQ (accessed August 6, 2022).

[16] P.A. Sheth, M. Neurock, M.C. Smith, First-principles analysis of the effects of alloying Pd with Ag for the catalytic hydrogenation of acetylene− ethylene mixtures, J Phys Chem B. 109 (2005) 12449–12466. https://doi.org/10.1021/jp050194a.

[17] Che, F., Zhang, R., Hensley, A. J., Ha, S., & McEwen, J. S, Density functional theory studies of methyl dissociation on a Ni (111) surface in the presence of an external electric field. *Physical Chemistry Chemical Physics* (2014), *16*(6), 2399-2410.

[18] Engelmann, Y., Mehta, P., Neyts, E. C., Schneider, W. F., & Bogaerts, A, Predicted influence of plasma activation on nonoxidative coupling of methane on transition metal catalysts. *ACS Sustainable Chemistry & Engineering* (2020), *8*(15), 6043-6054.